JOURNAL OF GEOPHYSICAL RESEARCH, VOL. 115, D13303, doi:10.1029/2009JD012654, 2010

The photochemistry of carbon monoxide in the stratosphere and mesosphere evaluated from observations by the Microwave Limb Sounder on the Aura satellite

K. Minschwaner,[1] G. L. Manney,[1,2] N. J. Livesey,[2] H. C. Pumphrey,[3] H. M. Pickett,[2] L. Froidevaux,[2] A. Lambert,[2] M. J. Schwartz,[2] P. F. Bernath,[4,5] K. A. Walker,[4,6] and C. D. Boone[4]

Received 15 June 2009; revised 19 February 2010; accepted 12 March 2010; published 14 July 2010.

[1] The photochemical production and loss rates for carbon monoxide (CO) in the stratosphere and mesosphere are evaluated using measurements from the Aura Microwave Limb Sounder (MLS) and the Atmospheric Chemistry Experiment-Fourier Transform Spectrometer (ACE-FTS). The distributions of reactive trace gases involved in the photochemistry of CO, including OH, CH_4, $O(^1D)$, Cl, as well as temperatures for calculating reaction rates, are either directly observed or constrained from observations. We map the CO net production and loss as a function of pressure (10–0.02 hPa, about 30–75 km altitude), latitude (approximately ±70°), and season. The results indicate that photochemical loss dominates over production for nearly all conditions considered here. A minimum photochemical loss lifetime of about 10 days occurs near the 2 hPa pressure level, and it follows the region of maximum sunlight exposure. At high latitudes during winter, the CO lifetime is generally longer than 30 days. Time scales become much shorter in spring, however, when CO lifetimes can be 15–20 days poleward of 60° latitude in the upper stratosphere. On the basis of these results, CO is a suitable tracer during autumn to spring above the 0.1 hPa pressure level but not in the upper stratosphere near 1 hPa.

Citation: Minschwaner, K., et al. (2010), The photochemistry of carbon monoxide in the stratosphere and mesosphere evaluated from observations by the Microwave Limb Sounder on the Aura satellite, *J. Geophys. Res.*, *115*, D13303, doi:10.1029/2009JD012654.

1. Introduction

[2] The distribution of carbon monoxide (CO) in the stratosphere and mesosphere has long been used to infer dynamical processes and diagnose trace gas transport [*Hays and Olivero*, 1970; *Allen et al.*, 1981]. This utility arises because the photochemical lifetime of CO is expected to be at least as long as the time scale for many of the dynamical problems of interest. Measurements of CO have thus become an important tool for understanding large-scale mesospheric circulations [*Clancy et al.*, 1984; *de Zafra and Muscari*, 2004; *Grossman et al.*, 2006] and vertical motions in the stratosphere and mesosphere [*Allen et al.*, 1999, 2000; *Forkman et al.*, 2005] and for evaluation of the dynamics in three-dimensional models [e.g., *Jin et al.*, 2005].

[3] Previous estimates for the photochemical lifetime of CO in the stratosphere and mesosphere were based on one- or two-dimensional models [e.g., *Allen et al.*, 1981; *Solomon et al.*, 1985] with values ranging between 5 and 50 days, depending primarily on altitude. Model-calculated CO lifetimes are limited by the ability of models to faithfully simulate the spatial and temporal behavior of trace species involved in the production and destruction of CO, with the most important of these being hydroxyl (OH) and methane (CH_4) [*Wofsy et al.*, 1972]. Thus, the relative contribution of photochemical effects in determining the overall distribution of CO has not always been easy to gauge. The photochemistry of CO in the middle atmosphere involves a relatively small set of reactions, however, that are now open to investigation using recent satellite data. For the first time, simultaneous measurements of most of the reactive species involved in the production and loss of CO are presently available from the Aura Microwave Limb Sounder (MLS) on the Aura satellite and from the Atmospheric Chemistry Experiment-Fourier Transform Spectrometer (ACE-FTS) on the SCISAT-1 satellite.

[4] Here we quantify the rates for CO photochemical production and loss in the upper stratosphere and mesosphere

[1]Department of Physics, New Mexico Institute of Mining and Technology, Socorro, New Mexico, USA.
[2]Microwave Atmospheric Science Team, Jet Propulsion Laboratory, California Institute of Technology, Pasadena, California, USA.
[3]School of Geoscience, University of Edinburgh, Edinburgh, UK.
[4]Department of Chemistry, University of Waterloo, Waterloo, Ontario, Canada.
[5]Department of Chemistry, University of York, Heslington, York, UK.
[6]Department of Physics, University of Toronto, Toronto, Ontario, Canada.

0148-0227/10/2009JD012654

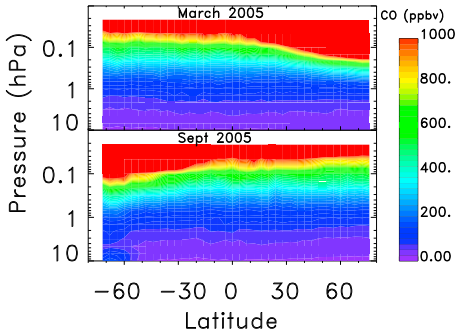

Figure 1. Zonal mean carbon monoxide mixing ratios measured by MLS and averaged over 15 day periods centered on the equinoxes. Data are version 2.2, daytime measurements for (top) March 2005 and (bottom) September 2005.

(between about 30 and 75 km) using simultaneously measured trace gas mixing ratios and temperatures from MLS. In cases where the targeted trace gas is not directly measured by MLS, we develop and test reliable proxies based on MLS and ACE-FTS measurements. The resulting production and loss rates are used to evaluate the photochemical lifetime of CO as a function of pressure, latitude, and season during 2005.

2. CO Photochemistry and Relevant Observations

[5] Carbon monoxide is produced near the Earth's surface from the oxidation of hydrocarbons (primarily isoprene and methane) and through combustion processes such as fossil fuel and biomass burning. Its concentration is highly variable in the troposphere, ranging between 50 and 100 ppb in uncontaminated air and increasing to at least 500 ppb in urban or biomass-burning plumes [*Sachse et al.*, 1988; *Barnes et al.*, 2003]. Tropospheric CO is transported into the stratosphere through convection and diabatic uplift in the tropical branch of the Brewer-Dobson circulation, as observed, for example, in the CO "tape recorder" signal from Aura MLS data [*Schoeberl et al.*, 2006].

[6] CO can also be produced within the stratosphere and mesosphere as an end product of the oxidation of methane, which is initiated by reactions with either OH, atomic chlorine (Cl), or atomic oxygen in its first excited state, $O(^1D)$,

$$\text{(R1)} \qquad CH_4 + OH \rightarrow CO + \text{products},$$

$$\text{(R2)} \qquad CH_4 + Cl \rightarrow CO + \text{products},$$

$$\text{(R3)} \qquad CH_4 + O(^1D) \rightarrow CO + \text{products}.$$

Production also occurs from the ultraviolet photodissociation of carbon dioxide (CO_2),

$$\text{(R4)} \qquad CO_2 + h\nu \rightarrow CO + O.$$

As a result primarily of CO_2 photodissociation, there exists a large reservoir of CO in the upper mesosphere and lower thermosphere (75–100 km) that can be transported down to lower altitudes, for example, during periods of strong descent at high latitudes during winter [*Solomon et al.*, 1985; *Allen et al.*, 2000].

[7] The photochemical loss of CO in the stratosphere and mesosphere is governed primarily by the oxidation reaction with OH to form CO_2,

$$\text{(R5)} \qquad CO + OH \rightarrow CO_2 + H.$$

MLS and ACE-FTS measurements can be used to evaluate rates for the set of reactions (R1)–(R3) and (R5), as discussed below. The latitudes for MLS observations range between 82°S and 82°N, although the latitude range for this analysis is somewhat more restricted and it varies with season, as CO production and loss rates are significant only during the daytime.

2.1. CO

[8] Carbon monoxide is retrieved from radiances observed by the MLS 240 GHz radiometer [*Pumphrey et al.*, 2007]. The useful range in pressure is from 215 to 0.0046 hPa, but for the purposes of this study, we focus on version 2.2 CO data between 10 hPa (~30 km) and 0.02 hPa (~75 km), where systematic uncertainties are estimated to range between 10% and 30%. Comparisons with ACE-FTS and ODIN-SMR show tendencies for positive biases in the MLS mesospheric CO data, which may be on the order of 25%. A small subset of the MLS CO data was excluded from the analysis due to the risk of contamination from galactic CO emission within the instrument field of view [*Pumphrey et al.*, 2008].

[9] Figure 1 shows zonal mean distributions of CO for March and September 2005. As discussed above, mixing ratios increase by an order of magnitude from the stratosphere to the mesosphere. The strong descent of air in the wintertime polar mesosphere and stratosphere transports high CO amounts into these regions, leading to a downward tilt of the CO isopleths toward the springtime hemisphere. The MLS CO data are used here to quantify the rate of loss (reaction (R5)) for the derivation of methane from MLS measurements (section 2.3) and for estimating the doubling lifetime (section 4). Uncertainties in measured CO do not impact the loss lifetime since this is independent of the CO concentration (section 4), but they do introduce errors in the doubling lifetime that are on the order of 25%.

2.2. O_3

[10] Ozone densities are not used directly in any calculations of CO production and loss, but they are required in order to determine OH diurnal variations and $O(^1D)$ concentrations using MLS measurements (sections 2.3 and 2.6). Version 2.2 stratospheric and mesospheric ozone profiles are measured using scans from the MLS 240 GHz radiometer [*Froidevaux et al.*, 2008a]. The estimated error in retrieved ozone is 5%–10% throughout the stratosphere, with larger uncertainties (up to 35%) possible in the mesosphere, where the uppermost range of useful data (0.02 hPa) corresponds to the top of our analysis. We assume constant ozone densities throughout the day, which is consistent with models and measurements that show relatively small (<10%) variations in O_3 about the daytime mean below 70 km altitude [*Schneider*

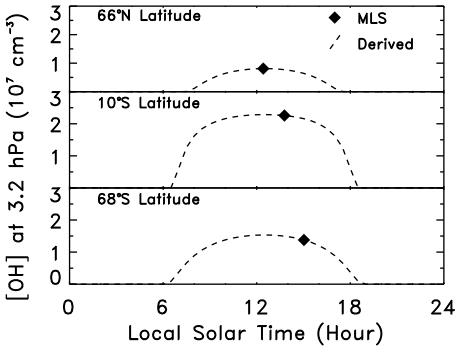

Figure 2. Hydroxyl concentrations measured by MLS (diamond symbols) at the 3.2 hPa pressure level in March 2005, at the indicated local solar times. Three measurements are shown at latitudes of (top) 66°N, (middle) 10°S, and (bottom) 68°S. Dashed curves for each MLS OH measurement show the parameterized OH diurnal variation from equation (1) using the coincident ozone column measured by MLS.

et al., 2005; *Huang et al.*, 2008]. The ozone is used here for UV fluxes, $O(^1D)$ densities, and OH diurnal variations, which are important only during daytime periods, thus large differences observed between daytime and nighttime mesospheric ozone do not impact our results. There are large temporal gradients of ozone around sunrise and sunset that can, however, introduce errors up to 4% in the CO lifetime.

2.3. OH

[11] Hydroxyl mixing ratios are measured using the MLS THz receiver [*Pickett et al.*, 2008]. The combined systematic errors in version 2.2 OH densities are less than 8% between 10 and 0.02 hPa. Comparisons between MLS OH and in situ measurements from two balloon flights show agreement to within 15% in the middle stratosphere. Larger differences are seen in comparisons with OH measured by the Middle Atmosphere High-Resolution Spectrograph Investigation (MAHRSI) in the upper stratosphere and mesosphere, although the MAHRSI data were taken during a different year.

[12] One difficulty in applying MLS OH data to calculate CO production and loss arises from the large diurnal variation in OH, coupled with the Sun-synchronous orbit of the Aura satellite. Maximum OH densities occur near midday throughout the stratosphere and lower mesosphere in response to the local actinic flux, and nighttime OH is practically negligible compared to daytime OH below 70 km [e.g., *Allen et al.*, 1984]. On the other hand, MLS daytime measurements are obtained at different local times depending on latitude due to the Aura orbit, thus latitudinal and diurnal effects are combined in the data. Untangling these effects requires an algorithm to infer the complete diurnal time variation of OH for each measurement point.

[13] Our approach to this problem involves an observationally constrained parameterization based on the primary production mechanism for OH: reaction of H_2O with $O(^1D)$. H_2O densities do not vary diurnally, but $O(^1D)$ densities are expected to be in photochemical steady state during the day and linearly proportional to the actinic flux that drives the photodissociation of O_3 (see section 2.6). The parameterization therefore follows a Beer-Lambert extinction relation,

$$[\mathrm{OH}](t) = [\mathrm{OH}]_o \exp(-0.5\tau_{O3} \sec[\Theta(t-\Phi)]), \quad (1)$$

where $[\mathrm{OH}](t)$ is the OH concentration as a function of time t, $[\mathrm{OH}]_o$ is the maximum concentration for the specific location and day, τ_{O3} is the ozone vertical optical depth, and Θ is the solar zenith angle corresponding to local time t, modified by a phase lag Φ. The factor of 0.5 accounts for the expected proportionality between the OH density and the square root of its production rate [e.g., *Canty and Minschwaner*, 2002], while the parameter Φ is set to 1/2 h to account for the approximate time constant for HO_x ($OH + HO_2 + H$) photochemistry in the upper stratosphere and mesosphere [*Li et al.*, 2005]. Note that equation (1) is based on photochemical equilibrium, but it includes a correction for departures from equilibrium through the phase lag parameterization and that it leads to a diurnal behavior which is not symmetric about noon. In addition, equation (1) is only appropriate for Θ less than about 70° due to the plane-parallel assumption.

[14] The parameters for equation (1) are determined separately for each MLS OH measurement at time t_m and pressure level p_m. First, τ_{O3} is calculated using the MLS ozone profile (section 2.2) measured above level p_m, multiplied by a mean O_3 absorption cross section of 1.2×10^{-18} cm^2. In this parameterization, temperature dependencies and quantum yields are neglected in favor of a simple and fast scheme that is optimized for computing the diurnal variation of UV penetration to the middle and upper stratosphere. Next, the secant of solar zenith angle is computed for the phase-shifted time ($t_m - \Phi$). Lastly, the MLS OH measurement $[\mathrm{OH}](t_m)$ provides a boundary condition needed to determine $[\mathrm{OH}]_o$, so that the complete diurnal cycle $[\mathrm{OH}](t)$ can be calculated using equation (1).

[15] Figure 2 shows an example of results from equation (1) at the 2.3 hPa pressure level for three different latitudes. These were chosen to represent the typical range of latitudinal variability due to three main factors: (1) the general level of OH constrained by the MLS measurement, (2) the overall diurnal pattern governed by midday Sun angle and length of day, and (3) the shape of the diurnal pattern impacted by the local overhead ozone column. A comparison with balloon-borne measurements [*Pickett et al.*, 2006; *Jucks et al.*, 1998] is shown in Figure 3 for 1 day and latitude. There is good agreement between the parameterized OH diurnal behavior and the balloon OH measurements throughout most of the day; however, it must be emphasized that the simplified parameterization cannot be expected to perform as well under all possible conditions. In particular, the mean ozone absorption cross section used for τ_{O3}, as discussed above, has been tuned to provide the best results for the pressure range 0.1–1.0 hPa and for an MLS OH boundary condition near Θ = 60°. This partly explains why early morning and late afternoon parameterized values are smaller than measured densities at 10 hPa (Figure 3), where the use of a smaller mean ozone cross section may be more appropriate. In addition, the parameterization applied to MLS measurements obtained at solar zenith angles greater than 80° can produce unrealistically large values of $[\mathrm{OH}]_o$, and these data are not included for calculating CO lifetimes. Uncertainties in diurnally averaged OH concentrations, which are used for both CO loss lifetimes

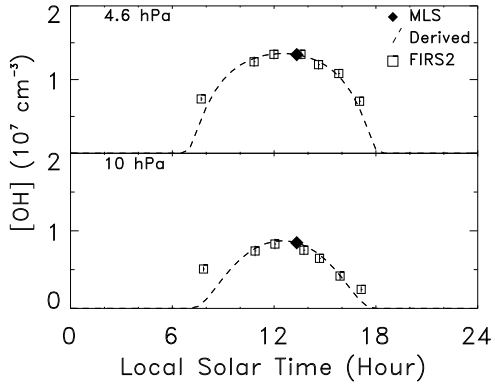

Figure 3. Hydroxyl concentrations (solid diamond symbols) measured by MLS at (top) 4.6 hPa and (bottom) 10 hPa on 23 September 2004, closest to the location of a balloon flight from Fort Sumner, NM (34.5°N, 104°W) [*Pickett et al.*, 2006]. Also shown are the derived OH values from equation (1) based on MLS (dashed curves) and balloon-borne measurements (open squares) from the Far Infrared Spectrometer (FIRS-2) instrument [*Jucks et al.*, 1998].

and doubling lifetimes (section 4), are estimated to be slightly larger than the ~10% systematic measurement error, ranging between 15% at 10 hPa to 25% at 0.02 hPa.

2.4. CH_4

[16] Methane plays an important role in the production of CO, but simultaneous observations of CH_4 with CO and OH are not consistently available, excluding a limited number of coincident measurements between MLS and other instruments that do observe methane. MLS measures water vapor (H_2O), however, and there are well-established relationships between stratospheric water vapor and methane [e.g., *Abbas et al.*, 1996]. Figure 4 shows the observed relationship between CH_4 and H_2O from ACE-FTS measurements. The data are version 2.2 retrieved from high resolution infrared absorption spectra during sunrise and sunset limb occultations [*Bernath et al.*, 2005; *Boone et al.*, 2005]. We included over 5000 limb profiles from 2005 observations, spanning the latitude range 85°S to 85°N between 30 and 70 km altitude.

[17] Throughout most of the stratosphere below 50 km altitude, methane and water vapor are nearly linearly related as a result of methane oxidation, such that the quantity $2CH_4 + H_2O$ is approximately constant [e.g., *Nassar et al.*, 2005]. In the mesosphere, however, both methane and water are destroyed by photolytic processes, and their relationship follows a different pattern in which both mixing ratios are decreasing rapidly with increasing altitude. This regime is also present within the polar stratosphere during winter, where transport is downward from the mesosphere. We found that the corresponding CO mixing ratio can be used to distinguish between the two regimes, as indicated in Figure 4. A CO mixing ratio of 120 ppbv provides a suitable threshold level for separating the different regimes, where each regime can then be represented using a polynomial fit of CH_4 as a function of H_2O, as shown in Figure 4.

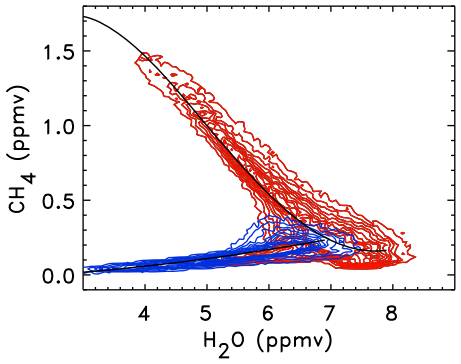

Figure 4. Point density contours of methane and water vapor mixing ratio measurements from ACE-FTS at all latitudes for 2005 and between 30 and 70 km altitude. Red contours denote data where the measured CO mixing ratio is less than 250 ppbv; blue contours correspond to CO mixing ratios greater than 250 ppbv. Solid curves are a fourth degree polynomial fit (for the red contours) and a second degree polynomial (for the blue contours).

[18] The standard MLS water vapor product used here is obtained from the 190 GHz retrieval. A systematic error analysis yields uncertainties in the range of 4%–9% for the altitude region of interest. Comparisons between MLS H_2O and other satellite platform measurements show very good agreement, with small differences between 5% and 10% in the upper stratosphere and mesosphere [*Lambert et al.*, 2007].

[19] Vertical profiles of MLS-derived methane within two latitude regions are shown in Figure 5, along with sunrise and sunset Halogen Occultation Experiment (HALOE) measurements [*Russell et al.*, 1993] for the same day and latitude ranges. The derived methane agrees well (within 20%) with HALOE in the middle stratosphere and lower mesosphere, including the representation of vertical gradients in mixing ratios that span nearly two orders of magnitude. There are larger differences in the upper stratosphere between

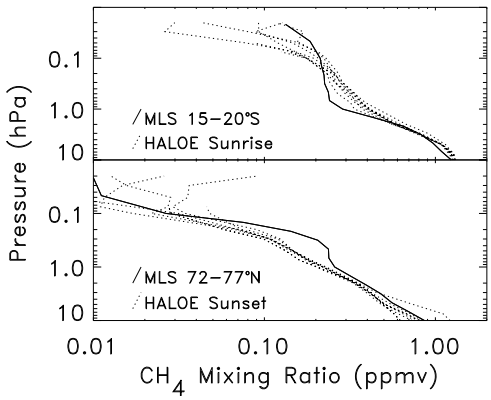

Figure 5. (top) CH_4 mixing ratios derived from MLS H_2O and CO, averaged between 15°S and 20°S latitude from 16 April 2005 (solid curve), along with HALOE CH_4 sunrise vertical profiles from the same day and latitude range (dotted curves). (bottom) Same as above but for the latitude range 72°N–77°N and for HALOE sunset data.

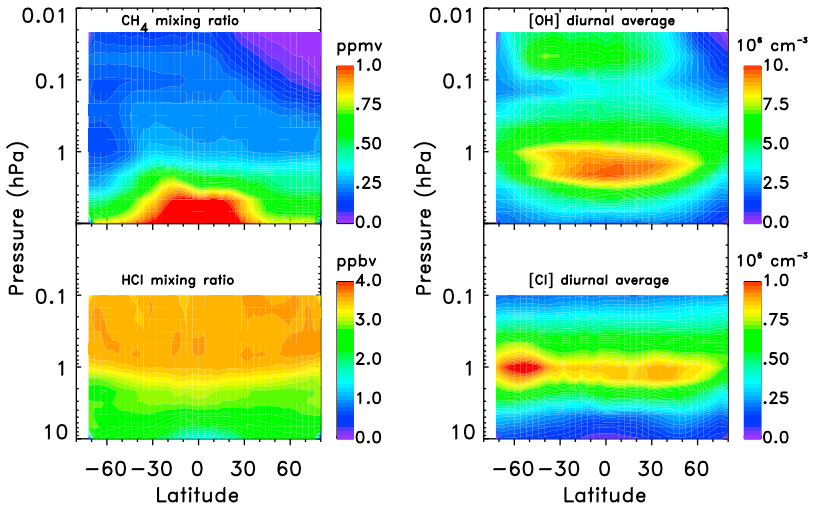

Figure 6. (top left) Zonal mean methane mixing ratios (parts per million volume) derived from MLS water vapor and carbon monoxide, averaged over a 15 day period centered on 22 March 2005. (top right) Zonal mean, diurnal average OH concentrations (10^6 molecules cm^{-3}) from MLS measurements for March 2005. (bottom left) MLS zonal mean HCl mixing ratios (parts per billion volume) for March 2005. (bottom right) Zonal mean, diurnal average Cl concentrations (10^6 molecules cm^{-3}) derived from MLS measurements for March 2005.

about 1 and 0.3 hPa that arise primarily from errors in the derived methane. The differences occur in a transition region where the two photochemical regimes from Figure 4 are merged (near 7 ppm H_2O, 0.2 ppm CH_4) and where the CH_4-H_2O relationship is less compact. The impact of such errors on the computed CO production rate is difficult to gauge because they vary in magnitude and sign from profile to profile, although additional comparisons with HALOE indicate that the errors rarely exceed 50% and are sometimes less than 20%. In addition, the calculated CO production from CO_2 photodissociation is as large as, or larger than, the CH_4 oxidation source in the upper stratosphere (see below), thus further reducing the overall error.

[20] Figure 6 shows the March 2005 zonal mean distribution of CH_4 derived from the ACE-FTS empirical relationship between CH_4, H_2O, and CO from Figure 4 and applied to MLS H_2O and CO measurements. The derived CH_4 shows an overall pattern that is similar to previous satellite observations [*Kumer et al.*, 1993; *Ruth et al.*, 1997]. Largest values are found in the equatorial lower stratosphere, a double peak structure appears in the upper stratosphere at low latitudes, and in the mesosphere the isopleths tilt downward from the fall to the springtime hemisphere. In addition, a localized reduction in CH_4 at the high-latitude summer/fall stratopause noted by Ruth et al. is evident in the MLS-based distribution (~60°S latitude, 1 hPa pressure).

2.5. Cl

[21] Atomic chlorine is another reactive species not directly observed by MLS, but it can be inferred from expected relationships between ClO_x and hydrochloric acid (HCl). Reaction (R2) is a major chemical production mechanism for HCl, with a more minor role played by the reaction $Cl + HO_2 \rightarrow O_2 + HCl$. The dominant loss mechanism for hydrochloric acid is $HCl + OH \rightarrow Cl + H_2O$. The relative abundances of Cl and HCl can be estimated from the equilibrium ratio in the upper stratosphere [see *Brasseur and Solomon*, 2005, equation 5.301],

$$\frac{[HCl]}{[Cl]} = \frac{k_2[CH_4] + k_7[HO_2]}{k_6[OH]}, \quad (2)$$

where k_2 is the rate for reaction (R2), k_6 is the reaction rate for HCl + OH, and k_7 is the reaction rate for $Cl + HO_2$. We use OH and CH_4 concentrations, as discussed above, and HCl measurements from MLS to obtain Cl concentrations using equation (2). In general, individual profiles of HO_2 from MLS are unsuitable for this analysis; however, the HO_2 term in the numerator of equation (2) is generally small compared with the CH_4 term. Monthly average HO_2 densities from MLS indicate that the $Cl + HO_2$ reaction contributes no more than 20% throughout most of the stratosphere. This minor contribution is estimated using measured OH from MLS, along with a mean altitude profile of the HO_2/OH ratio from monthly average MLS measurements. The ratio varies from about 4 in the middle stratosphere to about 0.6 in the lower mesosphere. Reaction rate coefficients in equation (2) and in all subsequent calculations are based on JPL Evaluation 15 [*Sander et al.*, 2006]. The temperature dependencies for all reaction rates are taken into account using MLS version 2.2 temperature measurements [*Schwartz et al.*, 2008].

[22] Hydrochloric acid is retrieved from emission lines observed with the MLS 640 GHz radiometer [*Froidevaux et al.*, 2008b]. The version 2.2 data used here have a conservative upper pressure limit at 0.15 hPa for single vertical profiles. As shown below, this limit does not significantly impact our analysis since the derived rate for reaction (R2) decreases rapidly above the upper stratosphere. The uncertainties in retrieved HCl are 10% or less between 10 and 0.15 hPa, and comparisons with coincident profiles from ACE-FTS show very good agreement (typically within +−5%) [*Froidevaux et al.*, 2008b].

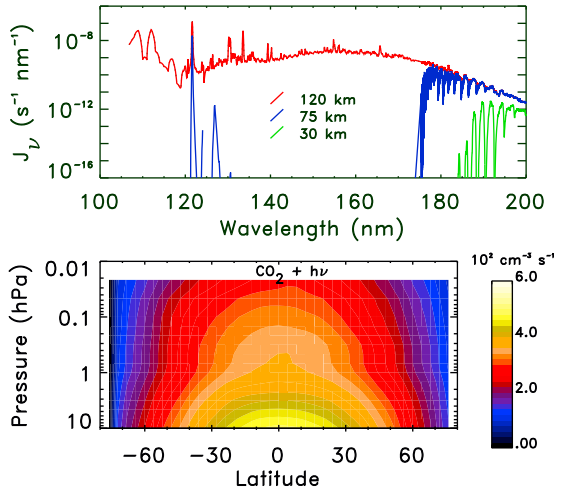

Figure 7. (top) Spectral photodissociation rates for carbon dioxide broken down into 1 nm intervals for a midlatitude summer atmosphere and solar zenith angle of 0°. Curves are shown at three altitudes: 120 (nearly zero optical path), 75, and 30 km. The 75 and 30 km curves correspond roughly to the top and bottom pressure levels, respectively, for this analysis. (bottom) Zonal mean CO_2 destruction rate ($J_{CO2} \times [CO_2]$) calculated for March 2005.

[23] Figure 6 shows the derived distribution of Cl for March 2005, along with the corresponding CH_4 (discussed above), HCl, and OH used in equation (2) for deriving Cl concentrations. For HCl, MLS measurements indicate a relatively flat distribution with latitude in comparison with the other trace gases and an increasing mixing ratio from the stratosphere to mesosphere. For OH, the diurnal average concentration displays a maximum in the low-latitude upper stratosphere with a secondary maximum in the mesosphere. The Cl vertical distribution follows its production from HCl + OH, but the latitudinal variation is strongly impacted by loss of ClO_x from reaction with CH_4. For example, a maximum in Cl near 1 hPa and 60°S appears to be driven by a corresponding minimum in CH_4.

[24] Concentrations of Cl in the stratosphere may also be estimated by assuming a steady state partitioning relationship between Cl and ClO [*Brasseur and Solomon*, 2005],

$$\frac{[\mathrm{ClO}]}{[\mathrm{Cl}]} = \frac{k_8[\mathrm{O_3}]}{k_9[\mathrm{O}] + k_{10}[\mathrm{NO}] + J_{\mathrm{ClO}}}, \tag{3}$$

where k_8 is the rate constant for $Cl + O_3 \rightarrow ClO + O_2$, k_9 is the rate constant for $ClO + O \rightarrow Cl + O_2$, k_{10} is the rate constant for $ClO + NO \rightarrow Cl + NO_2$, and J_{ClO} is the photodissociation rate for ClO. In principle, Cl can be derived using MLS measurements of ClO and O_3 along with values for (1) [O] from equilibrium partitioning between [O_3] and [O] (including a calculated ozone photolysis rate), (2) [NO] from either models or other measurements, and (3) calculated J_{ClO}. We calculated [Cl] from equation (3) using ACE measurements of NO for selected periods and latitudes that matched MLS observations of ClO and O_3 to test for consistency with Cl obtained from equation (3). In the middle stratosphere, the two methods generally agreed to within 30% with smaller Cl concentrations from equation (3) near 10 hPa and slightly larger values near 1.5 hPa. Equation (3) cannot be applied above the 1 hPa pressure level where the ClO measurement error becomes too large. In view of the limited availability of simultaneous NO measurements and the more restricted maximum altitude for measured ClO (1 hPa minimum pressure for ClO versus 0.15 hPa for HCl), equation (3) was not used for the CO photochemical budget analysis presented here.

2.6. O(^{1}D)

[25] The concentration of O(^{1}D) is calculated assuming photochemical steady state during the day,

$$[\mathrm{O}(^1\mathrm{D})] = \frac{J_{\mathrm{O3}}[\mathrm{O_3}]}{k_{\mathrm{N2}}[\mathrm{N_2}] + k_{\mathrm{O2}}[\mathrm{O_2}]}, \tag{4}$$

where J_{O3} is the photodissociation rate for ozone and k_{N2} and k_{O2} are quenching rate constants for collisions with N_2 and O_2, respectively. Ozone photodissociation is calculated using a radiative transfer code [*Minschwaner et al.*, 1993] with O_3 opacity and O_3 concentrations obtained from MLS data as discussed in section 2.2.

3. CO Production and Loss

[26] In addition to the methane oxidation reactions discussed above, we included photodissociation of CO_2 (reaction (R4)) in the overall production rate for CO. Photodissociation frequencies are calculated using high-resolution, temperature-dependent CO_2 cross sections measured by *Yoshino et al.* [1996] in the spectral region from 118 to 175 nm and by *Parkinson et al.* [2003] from 175 to 200 nm. At wavelengths below 118 nm, cross-section measurements of *Inn et al.* [1953] are used. The radiative calculations include temperature-dependent O_2 absorption cross sections and a detailed treatment of O_2 Schumann-Runge band absorption between 175 and 200 nm wavelengths [*Minschwaner et al.*, 1993]. Solar ultraviolet irradiances are taken from the Solar Ultraviolet Spectral Irradiance Monitor (SUSIM) measurements [*Brueckner et al.*, 1993].

[27] Figure 7 shows the spectral breakdown of CO_2 photodissociation at three altitudes for midlatitude summer conditions and $\Theta = 0°$. To our knowledge, this is the first application of the most recent high spectral resolution CO_2 cross-section measurements to calculations of CO_2 photodissociation in the terrestrial upper atmosphere. The CO_2 absorption cross section maximizes near 145 nm; consequently, the photodissociation rate (J_{CO2}) maximizes in the thermosphere where the continuum absorption by O_2 is weak. At lower altitudes, the dominant contribution to photodissociation occurs at wavelengths greater than 175 nm where the O_2 Schumann-Runge bands control the atmospheric opacity. A smaller contribution is contained within the Lyman-alpha spectral region near 121 nm. Photodissociation rates calculated here are about 50% larger than the results of *Wofsy et al.* [1972] at 10 hPa and 30°N latitude. At higher altitudes near the 0.1 hPa level, our values are 50% smaller than Wofsy et al.'s results but 50% larger than those presented by *Allen et al.* [1981]. On the basis of measurement uncertainties in CO_2 absorption cross sections (2%–5%) [*Yoshino et al.*, 1996; *Parkinson et al.*, 2003], solar ultraviolet fluxes (5%) [*Brueckner et al.*, 1993], and O_2 opacity (15%) [*Minschwaner*

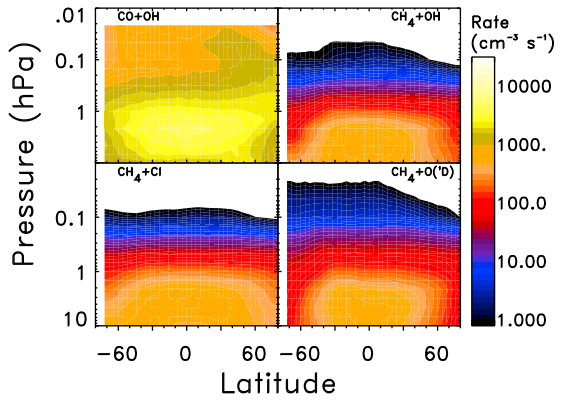

Figure 8. Diurnal average rates for CO production and loss derived from MLS measurements for March 2005. Rates are shown on a log scale for loss by (top left) reaction (R5), and production from (top right) reaction (R1), (bottom left) reaction (R2), and (bottom right) reaction (R3).

et al., 1993], we estimate associate uncertainties in the CO_2 photodissociation rate that vary from a maximum of 35% near 10 hPa to a minimum uncertainty of 20% near 0.02 hPa.

[28] Figure 7 also shows the diurnal averaged CO production rate from CO_2 photodissociation as a function of latitude and pressure. These are based on a constant, mean CO_2 mixing ratio of 368 ppm. Stratospheric production of CO from CO_2 photolysis is largest at low latitudes where solar zenith angles are smallest at midday. The production rate decreases from 500 cm^{-3} s^{-1} at 10 hPa to 200 cm^{-3} s^{-1} in the mesosphere. In comparison to the sources of CO from CH_4 oxidation (see below), this production is negligible in the middle stratosphere, but it is quite significant in the upper stratosphere and mesosphere.

[29] The derived rates for reactions (R1)–(R3) and (R5) in March 2005 are shown in Figure 8. The loss rate (reaction (R5)) maximizes in the stratosphere near the 2 hPa pressure level, following approximately the distribution of OH seen in Figure 6. In the mesosphere, however, the loss rate is larger in the Northern Hemisphere (springtime), which appears to be driven more by the mesospheric CO rather than by OH (cf. Figures 1 and 6). The three CO production rates shown in Figure 8 have a similar pattern with maxima confined to low latitudes and between 10 and 2 hPa. The reaction CH_4 + OH is the dominant production mechanism in the middle stratosphere, while the reaction CH_4 + $O(^1D)$ is more important at levels above the stratopause. The CH_4 + Cl reaction plays a minor role at all levels. The loss rate from reaction (R5) exceeds the sum of the production rates from reactions (R1)–(R4) for nearly all latitudes and pressures examined here, indicating that there is a net destruction of CO throughout most of the stratosphere and lower mesosphere.

4. CO Lifetimes

[30] The chemical continuity equation for CO can be written as

$$\frac{d[CO]}{dt} = P - L = [CH_4](k_1[OH] + k_3[Cl] + k_3[O(^1D)]) + J_{CO2}[CO_2] - k_5[CO][OH], \quad (5)$$

where P is the total production rate (first four terms on the right side of equation (5)) and L is the loss rate (last term in equation (5)), and the reaction rate coefficients and species concentrations are discussed above. A production lifetime defined by $\tau_P = [CO]/P$ represents an effective doubling time for the CO concentration. Similarly, a loss lifetime is typically defined by $\tau_L = [CO]/L$, where τ_L represents an e-folding time for destruction of CO. Although these two time scales appear mismatched, they do permit a comparison of net production versus net loss by a direct comparison of lifetimes, since they both involve the common term [CO]. For example, if τ_P exceeds τ_L by a factor of 2, it can be concluded that production is half as large as loss at that time and location.

[31] Figure 9 shows the distribution of lifetimes for March and September 2005. Consistent with the results from section 3, the loss lifetime is shorter than the production lifetime for all latitudes throughout most of the stratosphere and mesosphere. A minimum loss lifetime on the order of 10–15 days occurs in a broad region at low latitudes and midlatitudes in the upper stratosphere. The loss lifetime increases with height through the stratopause but decreases upward into the mesosphere, reaching 20 days at low latitudes near 0.3 hPa. One of the critical regions of interest is the high-latitude upper stratosphere, where the evolution of CO has been used to diagnose vertical motions within the polar vortex. In this regard, we find regions with CO loss lifetimes of 20 days or less within the upper stratosphere and poleward of 60° latitude, suggesting that CO densities may be significantly affected by photochemical effects during late winter and spring.

[32] Production lifetimes are more asymmetric with respect to latitude. In the stratosphere, the high-latitude spring hemisphere contains shorter production times, whereas in the mesosphere, the high-latitude spring hemisphere contains the longest production times. The hemispheric asymmetry is driven primarily by the derived distributions of methane (Figure 6). Note also that the coverage in latitude for computed lifetimes is different between the Northern and Southern hemispheres (values extend to higher latitudes in the NH). This arises from the asymmetry in local times for the Aura orbit between the Southern and Northern hemispheres and the

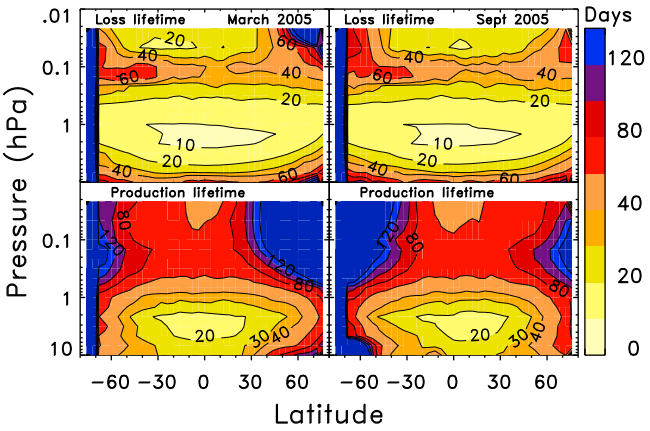

Figure 9. Zonally averaged time scales for photochemical (top) loss and (bottom) production for (left) March 2005 and (right) September 2005. Contour intervals are every 10 days from 0 to 40 days and every 20 days from 40 to 120 days.

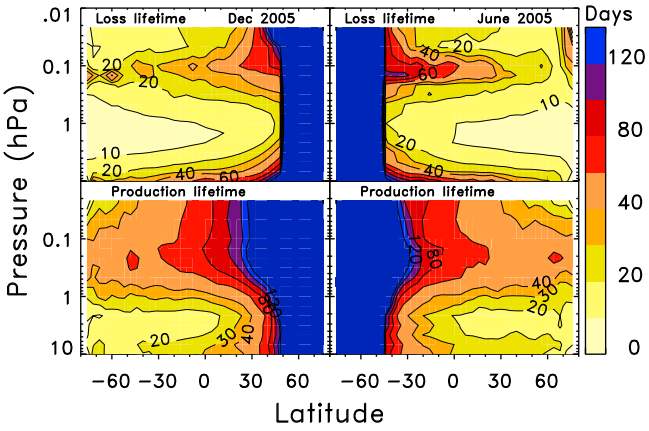

Figure 10. Same as Figure 9 but for (left) December 2005 and (right) June 2005.

fact that our analysis is limited to solar zenith angles of 80° or less for the diurnal variation in OH.

[33] Uncertainties in both loss and production lifetimes vary with latitude, pressure, and season according to the availability of solar ultraviolet radiation. In regions of total darkness, fractional uncertainties are very small since lifetimes are extremely long and CO is approximately conserved. An error budget for sunlit regions shows that the loss lifetime is a function of the temperature-dependent uncertainty in k_5 and of the uncertainty in diurnally averaged OH concentrations. Typical values for $\delta\tau_L/\tau_L$ at midlatitudes are 22% at 10 hPa, increasing to 31% at 0.02 hPa. The error budget for the production lifetime is more complicated due to the larger number of terms, but in the middle stratosphere, it is dominated by uncertainties in [CO], [CH_4], [OH], and k_1. Here we find typical values for $\delta\tau_P/\tau_P$ at midlatitudes to be 40% at 10 hPa. In the mesosphere where CO_2 photolysis is the dominant production mechanism, the uncertainty decreases to 32%.

[34] Figure 10 shows the corresponding lifetimes for the solstice seasons. Loss also dominates over production at the solstices, although in the high-latitude summer mesosphere, we find nearly comparable production and loss rates. As expected on the basis of the distributions of OH, CH_4, Cl, and $O(^1D)$, the shortest times for both loss and production occur in the summer hemisphere. In the winter hemisphere, contours are artificially terminated poleward of about 50° latitude due to the lack of daytime conditions, but the overall impact is small since lifetimes are tending toward very long values under these circumstances.

[35] In general, the vertical profile of CO loss lifetime found here is consistent with earlier published results for midlatitudes, with a primary minimum in the upper stratosphere and a secondary minimum in the mesosphere. Overall loss lifetimes are between 30% and 100% longer than model calculations for the upper stratosphere and mesosphere [*Allen et al.*, 1981; *Solomon et al.*, 1985], which is most likely related to differences in OH. *Canty et al.* [2006] found that OH concentrations observed by MLS were smaller than model results using standard kinetics between about 35 and 60 km altitude. The primary effect of changes in OH on the CO distribution is through the loss mechanism (reaction (R5)), so that reduced OH should lead to a longer loss lifetime and larger modeled CO [e.g., *Rusch and Clancy*, 1987]. For the lower and middle stratosphere, *Rinsland et al.* [2000] examined vertical profiles of CO from ATMOS (Atmospheric Trace Molecule Spectroscopy) and compared the measurements with photochemical steady state model calculations. At the 800 K potential temperature level, CO lifetimes of 37, 40, and 48 days were obtained for 0°N–20°N, 20°N–35°N, and 35°N–50°N, respectively. These values, valid for the ATMOS/ATLAS 3 observing periods near equinox conditions and at the bottom of our analysis range near 10 hPa pressure, are in fair agreement with the loss lifetimes shown in Figure 9.

5. Conclusions

[36] The photochemical budget of CO in the stratosphere and mesosphere was examined using satellite measurements from MLS and ACE-FTS. Carbon monoxide chemical loss is strongly linked to the altitude-latitude distribution and diurnal cycle of OH, which is driven by the intensity and duration of solar ultraviolet radiation exposure. A minimum photochemical loss lifetime of about 10 days occurs near the 2 hPa pressure level at low latitudes to midlatitudes during equinox. A secondary minimum of about 20 days occurs in the low-latitude to midlatitude mesosphere near 0.03 hPa. In comparison with previously modeled CO loss lifetimes, the shape of the vertical profile obtained here is similar but overall rates for photochemical loss are generally smaller, which is due primarily to the new constraints on OH obtained from MLS observations.

[37] During solstice, the minimum CO loss lifetime shifts to the mid- to high-latitude summer hemisphere, and at high latitudes in winter, the loss lifetime is generally much longer than 30 days throughout the stratosphere and mesosphere. It should be noted, however, that within the springtime high-latitude stratosphere the loss lifetime found here can fall below 20 days. This time scale could be important for the distribution of CO during the breakdown of the winter polar vortex, especially in the Antarctic where the polar vortex persists into late spring.

[38] The photochemical loss of CO exceeds production at nearly all latitudes and pressure levels examined. Production lifetimes are linked to the distributions of CH_4, OH, Cl, and O_3, as well as the photodissociation of CO_2. These all show considerable variation with pressure, latitude, and season, but on average the production lifetime is 40–60 days throughout most of the sunlit stratosphere and mesosphere.

[39] **Acknowledgments.** Work at the Jet Propulsion Laboratory, California Institute of Technology was done under contract with the National Aeronautics and Space Administration. This research was also supported by a Student Research Project subcontract 1278287 from JPL to NMT and by NASA grant NNX08AN78G to NMT. The ACE mission is funded primarily by the Canadian Space Agency. We thank Ken Jucks for providing FIRS-2 OH data.

References

Abbas, M. M., et al. (1996), The hydrogen budget of the stratosphere inferred from ATMOS measurements of H_2O and CH_4, *Geophys. Res. Lett.*, *23*(17), 2405–2408, doi:10.1029/96GL01320.

Allen, D. R., J. L. Stanford, M. A. Lopez-Valverde, N. Nakamura, D. J. Lary, A. R. Douglass, M. C. Cerniglia, J. J. Remedios, and F. W. Taylor (1999), Observations of middle atmosphere CO from the UARS ISAMS during the early northern winter 1991/1992, *J. Atmos. Sci.*, *56*, 563–583.

Allen, D. R., J. L. Stanford, N. Nakamura, M. A. Lopez-Valverde, M. Lopez-Puertas, F. W. Taylor, and J. J. Remedios (2000), Antarctic polar descent and planetary wave activity observed in ISAMS CO from April to July 1992, *Geophys. Res. Lett.*, *27*(5), 665–668, doi:10.1029/1999GL010888.

Allen, M., Y. L. Yung, and J. W. Waters (1981), Vertical transport and photochemistry in the terrestrial mesosphere and lower thermosphere (50–120 km), *J. Geophys. Res.*, *86*(A5), 3617–3627.

Allen, M., J. I. Lunine, and Y. L. Yung (1984), The vertical distribution of ozone in the mesosphere and lower thermosphere, *J. Geophys. Res.*, *89*(D3), 4841–4872.

Barnes, D. H., S. C. Wofsy, B. P. Fehlau, E. W. Gottlieb, J. W. Elkins, G. S. Dutton, and S. A. Montzka (2003), Urban/industrial pollution for the New York City–Washington, D. C., corridor, 1996–1998: 1. Providing independent verification of CO and PCE emissions inventories, *J. Geophys. Res.*, *108*, doi:10.1029/2001JD001116.

Bernath, P. F., et al. (2005), Atmospheric Chemistry Experiment (ACE): Mission overview, *Geophys. Res. Lett.*, *32*, L15S01, doi:10.1029/2005GL022386.

Boone, C. D., R. Nassar, K. A. Walker, Y. Rochon, S. D. McLeod, C. P. Rinsland, and P. F. Bernath (2005), Retrievals for the atmospheric chemistry experiment Fourier-transform spectrometer, *Appl. Optics*, *44*, 7218–7231.

Brasseur, G., and S. Solomon (2005), *Aeronomy of the Middle Atmosphere*, 3rd ed., Springer, Dordrecht.

Brueckner, G. E., K. L. Edlow, L. E. Floyd, J. L. Lean, and M. E. VanHoosier (1993), The Solar Ultraviolet Spectral Irradiance Monitor (SUSIM) experiment on board the Upper Atmosphere Research Satellite (UARS), *J. Geophys. Res.*, *98*, 10,695–10,711.

Canty, T., and K. Minschwaner (2002), Seasonal and solar cycle variability of OH in the middle atmosphere, *J. Geophys. Res.*, *107*(D24), 4737, doi:10.1029/2002JD002278.

Canty, T., H. M. Pickett, R. J. Salawitch, K. W. Jucks, W. A. Traub, and J. W. Waters (2006), Stratospheric and mesospheric HO_x: Results from Aura MLS and FIRS-2, *Geophys. Res. Lett.*, *33*, L12802, doi:10.1029/2006GL025964.

Clancy, R. T., D. O. Muhleman, and M. Allen (1984), Seasonal variability of CO in the terrestrial mesosphere, *J. Geophys. Res.*, *89*(D6), 9673–9676.

de Zafra, R. L., and G. Muscari (2004), CO as an important high-altitude tracer of dynamics in the polar stratosphere and mesosphere, *J. Geophys. Res.*, *109*, D06105, doi:10.1029/2003JD004099.

Forkman, P., P. Eriksson, D. Murtagh, and P. Espy (2005), Observing the vertical branch of the mesospheric circulation at latitude 60°N using ground-based measurements of CO and H_2O, *J. Geophys. Res.*, *110*, D05107, doi:10.1029/2004JD004916.

Froidevaux, L., et al. (2008a), Validation of Aura Microwave Limb Sounder stratospheric ozone measurements, *J. Geophys. Res.*, *113*, D15S20, doi:10.1029/2007JD008771.

Froidevaux, L., et al. (2008b), Validation of Aura Microwave Limb Sounder HCl measurements, *J. Geophys. Res.*, *113*, D15S25, doi:10.1029/2007JD009025.

Grossman, K. U., O. Gusev, and P. Knieling (2006), The distribution of carbon monoxide in the upper mesosphere and lower thermosphere during CRISTA-1 and -2, *J. Atmos. Sol.-Terr. Phys.*, *68*, 1764–1780.

Hays, P. B., and J. J. Olivero (1970), Carbon dioxide and monoxide above the troposphere, *Planet. Space Sci.*, *18*, 1729–1733.

Huang, F. T., H. G. Mayr, J. M. Russell III, M. G. Mlynczak, and C. A. Reber (2008), Ozone diurnal variations and mean profiles in the mesosphere, lower thermosphere, and stratosphere, based on measurements from SABER on TIMED, *J. Geophys. Res.*, *113*, A04307, doi:10.1029/2007JA012739.

Inn, E. C. Y., K. Watanabe, and M. Zelikoff (1953), Absorption coefficients of gases in the vacuum ultraviolet: Part III. CO_2, *J. Chem. Phys.*, *21*, 1648–1650.

Jin, J. J., et al. (2005), Co-located ACE-FTS and Odin/SMR stratospheric-mesospheric CO 2004 measurements and comparison with a GCM, *Geophys. Res. Lett.*, *32*, L15S03, doi:10.1029/2005GL022433.

Jucks, K. W., et al. (1998), Observations of OH, HO_2, H_2O, and O_3 in the upper stratosphere: Implications for HO_x photochemistry, *Geophys. Res. Lett.*, *25*(21), 3935–3938, doi:10.1029/1998GL900009.

Kumer, J. B., J. L. Mergenthaler, and A. E. Roche (1993), CLAES CH_4, N_2O, and CCl_2F_2 (F12) global data, *Geophys. Res. Lett.*, *20*(12), 1239–1242, doi:10.1029/93GL01341.

Lambert, A., et al. (2007), Validation of the Aura Microwave Limb Sounder middle atmosphere water vapor and nitrous oxide measurements, *J. Geophys. Res.*, *112*, D24S36, doi:10.1029/2007JD008724.

Li, K.-F., R. P. Cageao, E. P. Karpilovsky, F. P. Mills, Y. L. Yung, J. S. Margolis, and S. P. Sander (2005), OH column abundance over Table Mountain Facility, California: AM-PM diurnal asymmetry, *Geophys. Res. Lett.*, *32*, L13813, doi:10.1029/2005GL022521.

Minschwaner, K., R. J. Salawitch, and M. B. McElroy (1993), Absorption of solar radiation by O_2: implications for O_3 and lifetimes of N_2O, $CFCl_3$, and CF_2Cl_2, *J. Geophys. Res.*, *98*(D6), 10,543–10,561.

Nassar, R., P. F. Bernath, C. D. Boone, G. L. Manney, S. D. McLeod, C. P. Rinsland, R. Skelton, and K. A. Walker (2005), Stratospheric abundances of water and methane based on ACE-FTS measurements, *Geophys. Res. Lett.*, *32*, L15S04, doi:10.1029/2005GL022383.

Parkinson, W. H., J. Rufus, and K. Yoshino (2003), Absolute absorption cross section measurements of CO_2 in the wavelength region 163–200 nm and the temperature dependence, *Chem. Phys.*, *290*, 251–256.

Pickett, H. M., B. J. Drouin, T. Canty, L. J. Kovalenko, R. J. Salawitch, N. J. Livesey, W. G. Read, J. W. Waters, K. W. Jucks, and W. A. Traub (2006), Validation of Aura MLS HO_x measurements with remote-sensing balloon instruments, *Geophys. Res. Lett.*, *33*, L01808, doi:10.1029/2005GL024048.

Pickett, H. M., et al. (2008), Validation of Aura Microwave Limb Sounder OH and HO_2 measurements, *J. Geophys. Res.*, *113*, D16S30, doi:10.1029/2007JD008775.

Pumphrey, H. C., et al. (2007), Validation of middle-atmosphere carbon monoxide retrievals from the Microwave Limb Sounder on Aura, *J. Geophys. Res.*, *112*, D24S38, doi:10.1029/2007JD008723.

Pumphrey, H. C., R. E. Cofield, M. J. Filipiak, and N. J. Livesey (2008), An all-sky survey at 230 GHz by MLS on Aura, *Adv. Space Res.*, *43*, 342–348.

Rinsland, C. P., R. J. Salawitch, G. B. Osterman, F. W. Irion, B. Sen, R. Zander, E. Mahieu, and M. R. Gunson (2000), Stratospheric CO at tropical and midlatitudes: ATMOS measurements and photochemical steady state model calculations, *Geophys. Res. Lett.*, *27*(9), 1395–1398, doi:10.1029/1999GL011184.

Rusch, D. W., and R. T. Clancy (1987), Minor constituents in the upper stratosphere and mesosphere, *Rev. Geophys.*, *25*(3), 479–486.

Russell, J. M., L. L. Gordley, J. H. Park, S. R. Drayson, W. D. Hesketh, R. J. Cicerone, A. F. Tuck, J. E. Frederick, J. E. Harries, and P. J. Crutzen (1993), The halogen occultation experiment, *J. Geophys. Res.*, *98*(D6), 10,777–10,797.

Ruth, S., R. Kennaugh, L. J. Gray, and J. M. Russell III (1997), Seasonal, semiannual, and interannual variability seen in measurements of methane made by UARS halogen occultation experiment, *J. Geophys. Res.*, *102*(D13), 16,189–16,199.

Sachse, G. W., R. C. Harriss, J. Fishman, G. F. Hill, and D. R. Cahoon (1988), Carbon monoxide over the Amazon basin during the 1985 dry season, *J. Geophys. Res.*, *93*, 1422–1430.

Sander, S. P., et al. (2006), Chemical Kinetics and Photochemical Data for Use in Atmospheric Studies, Evaluation Number 15, JPL Publication 06-2, Jet Propulsion Laboratory, Pasadena.

Schneider, N., F. Selsis, J. Urban, O. Lezeaux, J. DelaNoe, and P. Ricaud (2005), Seasonal and diurnal ozone variations: Observations and modeling, *J. Atmos. Chem.*, *50*, 25–47.

Schoeberl, M. R., B. N. Duncan, A. R. Douglass, J. Waters, N. Livesey, W. Read, and M. Filipiak (2006), The carbon monoxide tape recorder, *Geophys. Res. Lett.*, *33*, L12811, doi:10.1029/2006GL026178.

Schwartz, M. J., et al. (2008), Validation of the Aura Microwave Limb Sounder temperature and geopotential height measurements, *J. Geophys. Res.*, *113*, D15S11, doi:10.1029/2007JD008783.

Solomon, S., R. R. Garcia, J. J. Olivero, R. M. Bevilacqua, P. R. Schwartz, R. T. Clancy, and D. O. Muhleman (1985), Photochemistry and transport of carbon monoxide in the middle atmosphere, *J. Atmos. Sci.*, *42*, 1072–1083.

Wofsy, S. C., J. C. McConnell, and M. B. McElroy (1972), Atmospheric CH_4, CO, and CO_2, *J. Geophys. Res.*, *77*(24), 4477–4493.

Yoshino, K., J. R. Esmond, Y. Sun, W. H. Parkinson, I. Ito, and T. Matsui (1996), Absorption cross section measurements of carbon dioxide in the wavelength region 118.7–175.5 nm and the temperature dependence, *J. Quant. Spectrosc. Radiat. Transfer*, *55*, 53–60.

P. F. Bernath, C. D. Boone, and K. A. Walker, Department of Chemistry, University of Waterloo, 200 University Ave. West, Waterloo, Ontario N2L 3G1, Canada.

L. Froidevaux, A. Lambert, N. J. Livesey, H. M. Pickett, and M. J. Schwartz, Microwave Atmospheric Science Team, Jet Propulsion Laboratory, California Institute of Technology, 4800 Oak Grove Dr., MS 183-701, Pasadena, CA 91109, USA.

G. L. Manney and K. Minschwaner, Department of Physics, New Mexico Institute of Mining and Technology, 801 Leroy Place, Socorro, NM 87891-4750, USA. (krm@kestrel.nmt.edu)

H. C. Pumphrey, School of Geoscience, Institute of Atmospheric and Environmental Sciences, University of Edinburgh, West Mains Rd., Edinburgh EH9 3JZ, UK.